



**Università degli Studi di Pavia**

---

FACOLTÀ DI SCIENZE MATEMATICHE, FISICHE, NATURALI  
Corso di laurea in Scienze Fisiche

**IDEA Dual-Readout calorimeter:  
Full simulation chain and neural network on particle ID**

Candidato  
**Alessandro Villa**  
Matricola 462495

Supervisore  
**Dott. Roberto Ferrari**  
Co-Supervisore  
**Dott. Lorenzo Pezzotti**



# Indice

<b>Introduction</b>	<b>iii</b>
<b>1 Future colliders</b>	<b>1</b>
1.1 Physics goals . . . . .	1
1.2 Leptonic colliders . . . . .	1
1.3 Hadronic colliders . . . . .	1
<b>2 IDEA Detector concept</b>	<b>3</b>
2.1 Vertex detector . . . . .	3
2.2 Drift chamber . . . . .	3
2.3 Magnet system . . . . .	3
2.4 Dual-readout calorimeter . . . . .	3
2.5 Preshower and muon chambers . . . . .	3
<b>3 Calorimetry and dual-readout</b>	<b>5</b>
3.1 Physics of shower development . . . . .	6
3.1.1 Electromagnetic Showers . . . . .	7
3.1.2 Hadronic showers . . . . .	7
3.2 Energy response of calorimeters . . . . .	7
3.2.1 Homogeneous calorimeters . . . . .	7
3.2.2 Sampling calorimeters . . . . .	7
3.2.3 Compensation . . . . .	7
3.3 Dual-readout calorimetry . . . . .	7
3.3.1 Working principles . . . . .	7
3.3.2 Experiments . . . . .	7
<b>4 Silicon Photomultipliers</b>	<b>9</b>
4.1 Working principles . . . . .	9
4.2 SiPM efficiency . . . . .	12
4.2.1 Occupancy effect . . . . .	14
4.3 Noise effects . . . . .	14
4.3.1 Dark Count Rate . . . . .	15
4.3.2 After-Pulse . . . . .	15
4.3.3 Optical Cross-Talk . . . . .	16

4.4	Timing properties . . . . .	17
<b>5</b>	<b>IDEA DR calorimeter full simulation</b>	<b>19</b>
5.1	Simulation structure . . . . .	20
5.1.1	Calorimeter simulation . . . . .	20
5.1.2	SiPM response digitization . . . . .	23
5.2	Simulation performances . . . . .	24
5.2.1	Different configurations . . . . .	24
5.2.2	Time studies . . . . .	24
5.2.3	Occupancy effect . . . . .	28
5.2.4	Energy resolution . . . . .	33
5.3	Neural Network: Particle ID on waveform . . . . .	40
5.3.1	Configuration . . . . .	40
5.3.2	Performances . . . . .	40
5.4	Neural Network: Particle ID on imaging . . . . .	40
5.4.1	Configuration . . . . .	40
5.4.2	Performances . . . . .	40
<b>6</b>	<b>Conclusion</b>	<b>41</b>
	<b>Thanks</b>	<b>43</b>
	<b>Bibliography</b>	<b>45</b>

# Introduction

aaa



# Capitolo 1

## Future colliders

aaa

### 1.1 Physics goals

aaa

### 1.2 Leptonic colliders

aaa

### 1.3 Hadronic colliders

aaa





## Capitolo 2

# IDEA Detector concept

aaa

### 2.1 Vertex detector

aaa

### 2.2 Drift chamber

aaa

### 2.3 Magnet system

aaa

### 2.4 Dual-readout calorimeter

aaa

### 2.5 Preshower and muon chambers

aaa



## Capitolo 3

# Calorimetry and dual-readout

Calorimetry is an important detection principle in particle physics. Originally developed with astrophysical purpose for cosmic-ray studies, this method refers to the detection of particles and the measurement of their properties, using blocks of instrumented material. It was developed and perfected for accelerator-based particle physics experimentation primarily in order to measure the energy of particles. In these blocks, particles are fully absorbed and their energy transformed into a measurable quantity.

The incident particle interact with the detector (through electromagnetic or strong processes) producing a shower of secondary particles with progressively degraded energy. The energy deposited by the charged particles of the shower in the active material of the calorimeter, which can be detected in the form of charge or light, is used to measure the energy of the incident particle. Typical processes suitable to detect this energy are: ionization of the medium, scintillation light and the Cherenkov light produced by relativistic particles.

Calorimeters can be divided into two categories depending on the type of shower they are optimized to detect: electromagnetic calorimeters, used mainly to measure electrons and photons through their electromagnetic interactions (e.g., bremsstrahlung, pair production), and hadronic calorimeters, used to measure mainly hadrons through their strong and electromagnetic interactions.

Another classification can be made according to their construction technique defining sampling calorimeters and homogeneous calorimeters.

Homogeneous calorimeters are built of one type of material that performs both the main tasks: degrade the energy of the incident particles and provide the detectable signal.

Sampling calorimeters, instead, consist of alternating layers of an absorber,

a dense material used to perform energy degradation, and an active medium that generate the signal.

Calorimeters are attractive in high-energy particle physic field for various reasons:

- In most cases the calorimeter energy resolution improves with energy as  $1/\sqrt{E}$ , where  $E$  is the energy of the incident particle. Therefore calorimeters are very well suited to high-energy physics experiments.
- Calorimeters are sensitive to all types of particles, charged and neutral (e.g., neutrons). Also neutrinos and their energy can be indirectly detected can even provide indirect detection of neutrinos and their energy through the measurement of the event missing energy.
- They are versatile detectors. They can be used to determine the shower position and direction, to perform particle identification, to measure the arrival time of the particle, or even to provide fast signals useful in trigger purpose.
- They are space and therefore cost effective. Because the shower length increases only logarithmically with energy, the detector thickness needs to increase only logarithmically with the energy of the particles.

This chapter describes the physics behind both the electromagnetic and hadronic shower developments, provides a basic description of the energy response of these detectors and introduces the particular technique of the dual-readout, a modern concept of calorimeter that has the quality of overcome the non-compensating problem producing both electromagnetic and hadronic showers measuring two different type of signal simultaneously (Cherenkov and scintillation light).

### 3.1 Physics of shower development

When a particle traverses matter, it will generally interact and lose (a fraction of) its en-ergy in doing so. The medium is excited in this process, or heated up, whence the term calorimetry. The interaction processes that play a role depend on the energy and the nature of the particle. They are the result of the electromagnetic (em), the strong and, more rarely, the weak forces reigning between the particle and the medium's constituents. In this chapter, the various processes by which particles lose their energy when traversing dense matter and by which they eventually get absorbed, are described. We also discuss shower development characteristics, the effects of

the electromagnetic and strong interactions, and the consequences of differences between these interactions for the calorimetric energy measurement of electrons and hadrons, respectively.

### 3.1.1 Electromagnetic Showers

aaa

### 3.1.2 Hadronic showers

aaa

## 3.2 Energy response of calorimeters

aaa

### 3.2.1 Homogeneous calorimeters

aaa

### 3.2.2 Sampling calorimeters

aaa

### 3.2.3 Compensation

aaa

## 3.3 Dual-readout calorimetry

aaa

### 3.3.1 Working principles

aaa

### 3.3.2 Experiments



## Capitolo 4

# Silicon Photomultipliers

SiPMs, also referred to as Multi Pixel Photon Counters (MPPCs) or Geiger mode Avalanche Photo-Diodes (G-APDs), are solid state light sensors featuring high internal gain, single-photon sensitivity, unprecedented photon number resolving capability, high Photon Detection Efficiency (PDE) and dynamic range, excellent time resolution, low bias voltage and magnetic field insensitivity. They represent an interesting alternative to the vacuum-based technologies thanks to their compactness, ruggedness, low cost and high-volume production capability. SiPMs benefit from the fast evolution of the silicon technology and the investment of different companies in terms of high quality mass production and design flexibility, enabling also a class of new applications spreading from the industrial and consumer technology sectors to fundamental research, as High Energy Physics (HEP). In this chapter, an overview of the main properties of these detectors will be provided, together with the description of the most important SiPM parameters and with some examples of applications in particle physics detectors.

### 4.1 Working principles

SiPM is a high density (up to  $10^4/mm^2$ ) matrix of Single-Photon Avalanche Diodes (SPADs), called pixels or cells, arranged on a common substrate with a common load and connected in parallel to a single readout output. The photo-diodes are usually p/n junctions, designed to be biased few volts above breakdown voltage ( $V_{Bk}$ ) in limited Geiger-Müller regime. Thanks to the high electric field in the depletion region, initial charge carriers generated by an absorbed photon (or by thermal effects) trigger an exponential charge multiplication by impact ionization. The process is stopped when the current spike across the quenching resistance induces a drop in the operating voltage. Thanks to its intrinsic charge amplification mechanism, requiring only a single carrier to detect the light pulse, SPAD features high single photon sensitivity. As a first order approximation, each diode provides the same

signal with  $\sim 10^6$  gain despite of the number of primary carriers generated. Thus the SiPM can be seen as a collection of binary pixels: by counting the number of fired cells it can provide information about the intensity of the incoming light. The typical SiPM cells size ranges between  $10 \times 10 \mu m^2$  and  $100 \times 100 \mu m^2$ , while the SiPM total areas from  $1 \times 1 mm^2$  up to  $6 \times 6 mm^2$  are available.

### Single photon avalanche diode

Fig. represents an illustrative picture of the SPAD doping structure: applying a reverse bias, the p-side is fully depleted and generates an electric field similar to that shown on the right side of the figure. The thin ( $0.1 - 1.5 \mu m$ ) n+ side receives the impinging photons through a window, while the multiplication region of high electrical field (in the order of few  $10^5 V/cm$ ) is placed between the n+ and p+ layers and is thin  $0.7 - 0.8 \mu m$ . Its nearly uniform field allows the electron-hole pairs separation and drifts them towards the n+ and p+ sides, respectively. When the drifting electron reaches the junction volume, it is accelerated by the high field and initiates the avalanche by impact ionization.

### Electrical model

The SPAD can be modelled as the circuit of fig.4.4: a parallel connection between the inner depletion region capacitance ( $C_D$ ) and the internal space-charge resistance of the avalanche region ( $R_S$ ). Each single photodiode has in series a quenching resistor ( $R_Q$ ). The current flowing through the switch is called  $I_{INT}$ , while the external current is the  $I_{EXT}$ .

Before photon detection, the switch is open (OFF condition) and  $C_D$  is charged to the bias voltage ( $V_{Bias}$ ). Upon an avalanche discharge, the switch is closed (ON condition) and the  $C_D$  capacitance discharges through the resistor  $R_S$  down to the breakdown voltage with a time constant  $\tau_D = C_D R_S$ .  $I_{INT}$  decreases exponentially from  $(V_{Bias} - V_{Bk})/R_S$  while  $I_{EXT}$  increases with the same time constant  $\tau_D$ . Both currents tend to the asymptotic value:  $(V_{Bias} - V_{Bk})/R_Q$ . In this phase the diode current is low (less than  $10 - 20 \mu A$ ), and a statistical fluctuation can quench the avalanche bringing the number of carriers in the multiplication region to zero. The switch is again open and the circuit returns in its initial OFF configuration.  $I_{INT}$  goes suddenly to zero, while  $I_{EXT}$  decreases exponentially. The capacitance  $C_D$  starts recharging to its original  $V_{Bias}$  with a time constant (called cell recovery time)  $\tau_r = C_D R_Q$ . Finally the SPAD is ready to detect a new photon. The easiest way to obtain a SPADs array is to connect them in parallel (building a SiPM). The SiPM current signal is the sum of the  $I_{EXT}$  coming from each SPAD fired by a photon and its amplitude and/or the signal charge are proportional to the impinging light intensity.



Fig. represents the current flowing during a discharge of a SPAD and its output signal time development.

Thanks to the very thin depletion layer and the extremely short avalanche discharge development duration, the SPAD response is intrinsically very fast. The signal rise time ( $< 500 \text{ ps}$ ) follows an exponential function with  $\tau_D$  time constant and does not depend on the number of fired cells and bias voltage applied. The falling signal is an exponential with time constant  $\tau_r$ . The total recovery time ranges between 20 and 250  $\text{ns}$ , accordingly to the quenching resistance value and to the cell size.

### Gain and amplitude

The gain of each SPAD represents the number of carriers flowing per each triggered avalanche. It is well defined by the internal capacitance and the integrated resistor and its average value is generally expressed as:

$$G = \frac{V_{Ov} C_D}{q} \quad (4.1)$$

where  $V_{Ov} = V_{Bias} - V_{Bk}$  is the excess bias with respect to the breakdown voltage at which the SiPM is operated and  $q = 1.602 \times 10^{-19} \text{ C}$  is the elementary charge. Fig. shows the typical SiPM response to a low-intensity, nanosecond long pulsed light, emitted by a LED, that conveyed few photons onto the sensor sensitive area. Each band of traces corresponds to a different number of fired cells. Since the typical gain value is high (in the order of  $10^6$  up to  $10^7$ ) compared to the noise level, traces are well separated, providing the good SiPM photon number resolving capabilities. It can be also estimated by the charge spectrum obtained integrating the SiPM signal, synchronous with the light pulses, over a certain time (fig.). Each entry corresponds to the recorded, digitized and integrated pixel current signal while each peak represents the number of cells with Geiger discharges at the same time (i.e. the number of fired cells). Their areas are related to the Poisson statistical property of the light source: the lowest peak corresponds to no detected photons and its width  $\sigma_0$  provides a measure of the stochastic fluctuations in the output signal (the noise of the system). The distance between two peaks, called peak-to-peak distance, is given by:  $\Delta_{pp} = q \cdot G$  and can be turned directly into the SiPM gain. Moreover, its value is the gauge to turn the digitised signal into the number of fired pixels. Usually the multi-photon spectrum is also shown in units of photoelectrons (pe), by scaling the ADC channels axis by  $1/\Delta_{pp}$  and shifting the first peak mean value at zero. The peak at one photo-electron has a slightly larger width  $\sigma_1$ . This is related to the fact that, even if the pixel structure production is high uniform, not all of the cells were born equal: the avalanches generated in various pixel scan have a difference of about 10% in the number of electrons generated (the so

called cell-to-cell gain variation).

Since the distribution of the fired cells in the SiPM sensitive area is random, the residual gain differences become evident broadening the peak and adding an extra contribution with respect to the 0 peak width. The peak width increases with the number of fired cells ( $N_{FC}$ ), following a  $N_{FC}$  law and limiting the maximum number of resolved peaks. The same information can also be extracted if, instead of the charge, the SiPM signal amplitude is analysed.

## 4.2 SiPM efficiency

Since each specific application can have various requirements in terms of wave-length sensitivity, the Photon Detection Efficiency is one of the first parameters to consider designing a SiPM-based readout detector. The silicon light absorption coefficient varies by several order of magnitude in the wavelength range from UV to infrared light (IR).

PDE quantifies the probability of a SiPM to detect an impinging photon and is defined as the ratio between the number of fired cells and the total number of photons hitting the detector  $N_\gamma$ . It is a function of the wavelength  $\lambda$  of the incident photon, of the temperature  $T$  and of the overvoltage  $V_{Ov}$  and can be calculated as:

$$PDE = \frac{\langle N_{FC} \rangle}{N_\gamma} = FF \cdot QE(\lambda) \cdot P_T(\lambda, V_{Ov}, T) \quad (4.2)$$

where  $FF$  is the geometrical fill factor (i.e. the ratio between the sensitive and the total device area),  $QE$  is the quantum efficiency (i.e. the probability for a photon with wavelength  $\lambda$ , to enter in the sensitive SiPM area and to create a primary  $eh$  pair) and  $P_T$  is the avalanche breakdown triggering probability (i.e. the probability that the carriers generates a Geiger discharge). Fig. is a sketch that shows how each factor of eq. 4.2 modifies the PDE. Starting with a PDE equal to 1, since the  $FF$  is (as first approximation) wavelength independent, it gives a first constant reduction.  $QE$  gives the second PDE wavelength dependent decrease. Finally, last reduction comes from the  $P_T$ .

### Geometrical fill factor

The geometrical fill factor is the ratio between the sensitive area and the total area of the device. It is linked to the presence of dead regions in the SPAD structure (fig. 4.10): each cell is surrounded by the guard ring (to quickly decrease the electric field at the border), the quenching resistors, the bias lines and the isolation structure providing the electrical and optical separation between the cells. One of the most used technique is trench isolation:

a narrow and depleted region surrounding the active area and blocked up with a dielectric layer. This allows a strong reduction of the optical cross-talk (sec.4.3.2) between the cells, especially if some absorbing material is inserted in the trench between the two dielectric layers. Both the trench isolation and the guard ring are usually designed together to minimise their width and to maximise the  $FF$ . This parameter has to be optimised for each specific application: e.g. if the number of impinging photons is small, the best solution can be using SiPM with few bigger cells (i.e.  $100\ \mu m$  pixel size), while in case of a high number of photons expected, SiPMs with small pixel sizes ( $10 - 25\ \mu m$ ) are needed to avoid saturation. Currently,  $FF$  ranges from 90% for  $100\ \mu m$  down to 30% for  $10\ \mu m$  pixel pitch.

### Quantum efficiency

The SiPM quantum efficiency depends on the wavelength of the impinging photon and on the absorption region thickness (fig.4.11). More in detail,  $QE$  depends on two factors: the probability that a photon crosses the anti-reflective coating (ARC) layer on top of the sensor and the one that a photon generates an  $eh$  pair in the high-field region. The ARC is usually composed by a stack of different dielectric layers on top of the SiPM and should be optimised for each application. The second probability depends on the absorption depth of photons in silicon, that grows with the wavelength from  $\sim 10\ nm$  range for the UV/blue light, up to tens of microns for the near-infrared (NIR) light. The thickness of the active region has to be adequately chosen according to the wavelength specific for each application. Considering a  $n+/p$  ( $p+/n$ ) junction, for very short wavelengths photons, the absorption depth is really small, the  $eh$  pairs are mainly photo-generated above the junction and only holes (electrons) are drifted towards the avalanche region. In this case a proper design of that layer is needed to allow the carriers diffusion towards the avalanche region and to minimise there combination. Instead, for visible part of the spectra, light is absorbed both above and below the high field region and thus both carriers can trigger the avalanche. Finally, NIR photons generate mostly electrons (holes) that trigger the avalanche below the junction. Since the two junction types generate different types of carriers triggering the avalanche, even considering the same  $QE$  and the same structure of the device, a difference PDE spectral shape is expected.

### Avalanche breakdown trigger probability

The avalanche breakdown trigger probability  $P_T$  is the probability that a carrier starts an avalanche passing through the SPAD high-field region. It depends on the electric field, i.e. on the overvoltage and on where the carriers

are produced. When an  $eh$  pair is created in the depletion region, the two carriers starts to drift in opposite direction, both contributing to the trigger probability:

$$P_T = P_h + P_e - P_h P_e, \quad (4.3)$$

where  $P_h$  and  $P_e$  are the hole and electron breakdown initiation probabilities. These terms depend on the generation position, are governed by the ionisation rates of holes and electrons, respectively, increase with the electric field and with low temperature. Electrons trigger the avalanche in a most efficient way because they have an impact ionization rate of  $5 \times 10^5 \text{ V/cm}$ , about twice higher than holes. Fig.4.12 represents the triggering probability as a function of the carrier generation depth both for n+/p and p+/n configurations.  $P_T$  has its maximum where the electrons can cross entirely the high-field zone: for the p+/n structure it is within the p+ layer near to the junction, while for the n+/p case it is the drift region  $\pi$ . In case of very short wavelength, i.e. for UV/blue light, the best solution is a buried n+/p structure. In this case electrons are generated near to the p+ layer and can enter in the high-field region, while holes move towards the electrode and do not contribute to the  $P_T$ . When moving to the green-red light detection (that have an absorption depth in silicon of about  $3 \mu\text{m}$ ) the best option is a p-type structure with a thin n+ layer ( $\sim 0.1 - 1.5 \mu\text{m}$ ) and a thicker drift region ranging from 3 to  $10 \mu\text{m}$ . For the NIR light, since the thickness of the high-field area is negligible with respect to the absorption depth, the proper choice is always a n+/p junction with illumination that can be from both the drift or the junction side.

#### 4.2.1 Occupancy effect

aaa

### 4.3 Noise effects

The main sources of the SiPM noise can be distinguished in two general categories called primary and correlated noise. The first category identifies the avalanche triggered by thermal generated free carriers or to the field-assisted generation (i.e. by tunneling generation). The correlated noise identifies all the avalanches discharges triggered in the SiPM by the primary ones, thus "correlated". The generation of these pulses is due to both the optical cross-talk(sec.) in neigh boring SiPM cells and the after-pulsing (sec.) in the same cell.

### 4.3.1 Dark Count Rate

The primary noise source, that limits the SiPM single photon resolution, is the Dark Count Rate (DCR). It is due to the avalanche triggered by any generation of  $eh$  pair in the depletion region, resulting in random and spurious avalanches that occur independently from the incoming light. Fig.4.13 shows the main sources of DCR along the SPAD depth. At room temperature, the main contribution is due to the thermal generation of the carriers in the band gap, i.e. the Shockley-Read-Hall (SRH) generation-recombination. The impurities and crystal defects of the epitaxial layer (in terms of number of activation energy and deep levels) define the generation rate: with a higher defect concentration, the equivalent "lifetime" ( $\tau_{SRH}$ ) becomes lower and thus the DCR increases. So, the sensor design and production technology play a crucial role to limit the dark count rate. SRH is also affected by the electric field present in the avalanche region. Fig.4.14 represents the temperature dependence of the DCR. On one hand, at higher temperature, the diffusion current near the depleted regions (from the neutral ones) becomes not negligible too. On the other hand, at lower temperature, the tunneling generation becomes more important and it is the dominant effect in the cryogenic applications. DCR is also depending on the total active area and on the depletion region thickness. To reduce as much as possible the DCR, the SiPM has to be operated at low bias voltage and temperature, employing small area devices. The actual values (at room temperature) for DCR range from 1  $MHz$  for the  $6 \times 6 \text{ mm}^2$ , to about tens of  $kHz$  for the  $1 \times 1 \text{ mm}^2$ , depending on the producer.

### 4.3.2 After-Pulse

After-pulsing (AP) is a correlated noise generated when the carriers produced in an avalanche are trapped by an impurity in the high-field region and subsequently released after a time that spreads from  $ns$  up to several  $\mu s$ , generating (on the same pixel) a delayed secondary avalanche [112]. Thus, the AP probability depends on the sensor technology, i.e. on the number of traps and impurities present in the silicon lattice and on their (multi-exponential [107]) release time constant compared to the pixels recovery time  $\tau_r$ . It is also depending from the overvoltage because, when the gain increases, the correspondent avalanche trigger probability increases too. The general procedure to reduce this kind of correlated noise is to minimise the gain and the silicon impurities and to find an adequate hold-off cell time that allows the majority of traps to be released when the pixel is not yet completely recharged. AP can also be "optically-induced": secondary photons produced by an avalanche can be re-absorbed in the neutral region of the same cell below the active region (fig.4.18). Then, the carrier can reach the avalanche region

by diffusion and trigger a new discharge. For this kind of AP, the carrier lifetime in the neutral region corresponds to the trap release time constant of the previous one and in the substrate this ranges between few to hundred of ns [126]. The optically-induced AP can be reduced using a low-lifetime substrate compared to the pixel recharged time constant or introducing a second p/n junction to block all the carriers coming from the backside [127]. Fig.4.19 summarises the SiPM output signal of the different noise sources: primary, prompt and delayed OCT and afterpulsing events.

### 4.3.3 Optical Cross-Talk

The number of secondary photons produced in an avalanche has been measured to be about  $3 \times 10^{-5}$  per charge carrier crossing the junction: with a SiPM gain of  $10^6$ , about 30 visible photons are generated during a cell break-down avalanche. These secondary photons are emitted isotropically and can be absorbed in the active volume of a neighbouring cells, triggering secondary avalanches resulting in a SiPM output pulse with two or three times the single-pixel amplitude (fig.4.15). This phenomenon is called "direct" or "prompt" Optical Cross-Talk (OCT) since the sum of the travel time of the photon from the first to the second pixel, the carrier drift time and the time needed to trigger the secondary avalanche is tens of picosecond and thus not distinguishable from the first avalanche with typical electronics. In addition to this, another type of OCT exists: the "delayed" OCT. It is caused by secondary photons generating an  $eh$  pair in the bulk or in the neutral regions next to the depleted area (fig.4.16). The generated carriers can diffuse to the active region and trigger a new avalanche. Another possible origin of OCT comes from photons exiting the silicon and reflected back in the avalanche region by e.g. the change of material reflective index fig.4.16. This can be defined as External OCT. Two examples of external reflector are the top surface of glass/resin layer added in some SiPM to protect the detector surface from environmental and mechanical stresses or a scintillator with diffusing/reflective surfaces. Contrary to prompt OCT, in this case the secondary avalanche production time can be long enough (from few  $ns$  up to  $\mu s$ ) to separate it from the starting time of the primary one and thus to identify two different and subsequent events. Anyway, due to the finite bandwidth and sampling rate available in the front-end and in the SiPM signal acquisition, part of the delayed OCT events can be identified as prompt OCT. Fig.4.17 shows an example of the DCR and OCT events frequency for a SiPM: higher order OCT decreases rapidly with the number of fired cells. The probability of simultaneously triggering  $N$  avalanches due to the optical cross-talk can be described exponentially decreasing with  $N$ . Often this simple model is sufficient and can be used to phenomenologically include OCT in Monte Carlo simulations. However, this is a very simple, first order approximation, model and a more complex and exhaustive description

of the OCT probability as a branching Poisson process can be found in [123] and in [124]. OCT increases with higher bias voltage: increasing the  $V_{Bias}$ , the number of photons produced during the avalanche increases and a larger triggering probability is expected. The OCT probability increases also reducing the SiPM pixel pitch due to the less average distance that photons have to travel before reaching the neighbour cells. Nowadays, to reduce properly the OCT down to a value of 1 – 2%, optical trenches between the SiPM pixels are inserted [125].

## 4.4 Timing properties

aaa





## Capitolo 5

# IDEA DR calorimeter full simulation

As already said, the concept described in chapter 2 is an on-going project and it has to be supported by simulation. With this goal, a dual-readout calorimeter full simulation has been developed allowing to generate data and monitor the whole process from the collision on the interaction point to the digitized signal produced by SiPMs.

The chapter presents a description of the simulation structure. The section 5.1 describes in details the simulation dividing it in two main Monte Carlo processes:

- the calorimeter simulation, coded in GEANT4;
- the SiPM response digitization (“pySIPM”), coded in Python.

Later, the performances obtained will be shown. The temporal behavior, the SiPM saturation effect and the energy resolution will be described in section 5.2.

Then the chapter treats of the possibility of simple particle identification using neural network structures.

The last section (sec.5.4) exposes a neural network that has the purpose of identify if signal are generated from photons ( $\gamma$ ) or neutral pions ( $\pi^0$ ). This aim is achieved analyzing the spatial pattern of energy released in the calorimeter.

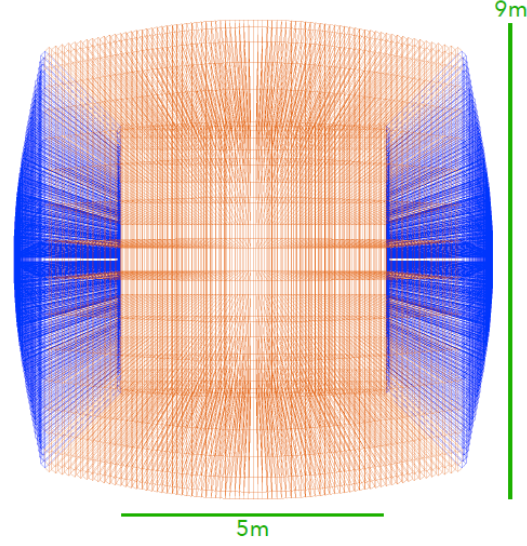


Figura 5.1: Calorimeter geometry.

## 5.1 Simulation structure

### 5.1.1 Calorimeter simulation

The calorimeter simulated follows the idea show in chapter 2. As can be seen, it has a cylindrical symmetry characterized by a barrel and two endcaps. This  $4\pi$  structure is obtained rotating 36 simpler component, called slices, around the  $z$  axis. The dimensions of the slices are shown in figure 5.2, therefore the inner diameter and the inner length are both 5  $m$  meanwhile the overall outer diameter and length are 9  $m$ .

Each half slice is composed by 75 2  $m$  long towers (40 part of the barrel and 35 part of the endcap), 5400 of this element are used to set up the whole calorimeter. To correctly cover an almost  $4\pi$  solid angle each tower has different trapezoidal inner face with dimensions that can vary from  $\sim 5$   $cm$  to  $\sim 8$   $cm$ . A small circular area, with 0.25  $m$  of radius, centered along the  $z$  axis is not covered by the calorimeter to permit the beam to reach the interaction point (IP).

The towers are copper based and play the role of absorber. To have a sensitive element they are filled by optical fibres. The idea of a projective calorimeter make the absorber volume greater increasing the distances from the IP. New fibres at different depth have to be placed inside the calorimeter to keep constant the sampling fraction.

As the dual-readout technique needs to distinguish Scintillating ( $S$ ) and Cherenkov ( $C$ ) signal, two types of fibres are used (fig. 5.3). Their charac-

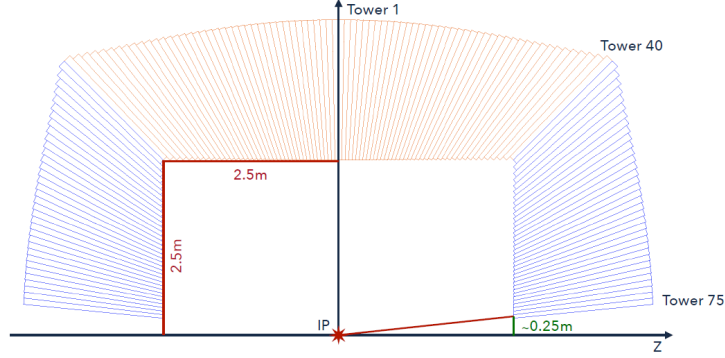


Figura 5.2: Calorimeter single slice.

<b>Kuraray SCSF-78 (<i>S</i>)</b>	
Core:	$r = 0.485 \text{ mm}$ , Polystyrene ( $C_5H_5$ ), $\rho = 1.95 \text{ g/cm}^3$ , $n = 1.59$
Cladding:	Thickness = 2% of $r$ , PMMA ( $C_5H_8O_2$ ), $\rho = 1.19 \text{ g/cm}^3$ , $n = 1.49$
Main properties:	Emission constant = $2.8 \text{ ns}$ , LY = $10^4 \text{ photons/MeV}$ , $\lambda_{att} = 4 \text{ m}$
<b>Mitsubishi SK-40 (<i>C</i>)</b>	
Core:	$r = 0.485 \text{ mm}$ , PMMA ( $C_5H_8O_2$ ), $\rho = 1.19 \text{ g/cm}^3$ , $n = 1.49$
Cladding:	Thickness = 2% of $r$ , Fluorinated Polymer ( $C_2F_2$ ), $\rho = 1.43 \text{ g/cm}^3$ , $n = 1.42$
Main properties:	$\lambda_{att} = 8.9 \text{ m}$

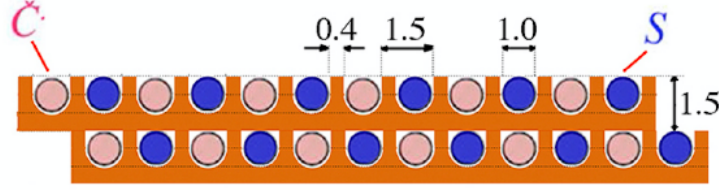
Tabella 5.1: fibres *S* and *C*.

teristic are shown in tab. 5.1.

The fibre refractive indices determine the light transport (as consequence of the Snell's law [2]). The signal from the scintillating fibres is parametrised by the deposited energy while the Cherenkov photons are produced accordingly to the Cherenkov emission process.

For each event, the simulation gives as output useful information:

- Event ID;
- Fibre Type;
- Fibre ID;
- the position of the fibre end closer to the IP;

Figura 5.3: Fibres  $C$  and  $S$ .

- the number of photons reaching the fibre further end;
- the list of photons time of arrival to the fibre end.

The computation of light propagation is extremely time consuming, so that it has to be fine tuned to optimize the process. In particular, the propagation of  $C$  photons is tracked until the single photon reach the core-cladding boundary (i.e. at the distance  $R$  from the further end of the fibre and at the time  $t_0$ ). If the emission angle is inside the range of the fibre numerical aperture, the photon is added to the final number of photons (after a Poissonian smearing on their number). The time of arrival on the sensor for each photon is estimated as:

$$t_C = t_0 + R \frac{n_C}{c} \quad (5.1)$$

where  $n_C = 1.49$  is the fibre refractive index and  $c$  is the speed of light.

The  $S$  fibres, instead, carry scintillating photons produced considering the light yield of the fibres and the energy deposited by the interacting particle. The number of photons is smeared with as Poissonian law and de time of arrival on the sensor is obtained as:

$$t_S = t_0 + R \frac{n_S}{c \times \cos(\vartheta)} + t^* \quad (5.2)$$

where  $n_S = 1.59$  is the refractive index and  $t^*$  is a random time that considers the fibres decay time, it is chosen from an exponential distribution with  $2.8 \text{ ns}$  as mean value. Considering the internal reflection, the photon path depends on the  $\vartheta$  angle (i.e. the angle between the photon direction and the fibre axis). It is chosen randomly in the range  $[\cos(\alpha), \cos(0)]$ , where  $\alpha = 20.4^\circ$  is the fibre critical angle.

Eventually, the light produced is smeared by two Poissonian distribution, one for scintillation photo-electrons and the other one for Cherenkov photo-electrons. This procedure correctly reproduces statistic fluctuations in scintillation and Cherenkov light production and allows to reproduce within simulations the scintillating light yield (p.e./GeV) desired. To make the full

simulation lighter, this process also includes the attenuation due to the PDE of the simulated SiPMs. The simulation is tuned to produce  $\sim 400 \text{ Spe/GeV}$  and  $\sim 100 \text{ Cpe/GeV}$  at the electromagnetic scale.

### 5.1.2 SiPM response digitization

The results obtained are the input of the second part of the simulation: *pySiPM*, a Monte Carlo simulation, performed mostly in Python, able to reproduce the SiPM response to a light source and replicate the waveforms recorded with a digitizer [3].

The importance of this software goes beyond our context, but perfectly fits our needs. In particular each fibre from the calorimeter simulation is considered coupled to a single SiPM, which digitized response is simulated through *pySiPM*.

The simulation allows to set most of the SiPM parameters:

- **Geometrical parameters:** the sensor dimensions and the pixel pitch.
- **Sensor parameters:** Photon Detection Efficiency, Dark Count Rate, After-Pulse probability, Optical Cross-Talk probability.
- **Signal parameters:** rise time constant, decay time constant.
- **Waveform parameters:** time window, sampling time, integration window.

For each event and fibre, random parameters determine the photon position inside the sensor. Meanwhile the sensor PDE is set at 100% to be consistent with the smearing applied at the calorimeter simulation level. A control stop the count of impinging photons on the same cell to a maximum one, then each element of noise is generated with the set probability.

The pulse generated is a combination of two exponentials characterized by the rise time constant ( $\tau_{rise}$ ) and the decay time constant ( $\tau_{fall}$ ), considering the different photon time of arrival ( $t_S$  and  $t_C$ ):

$$y(t) = A \cdot \left( e^{-\frac{t}{\tau_{fall}}} - e^{-\frac{t}{\tau_{rise}}} \right). \quad (5.3)$$

The total signal of each SiPM is the sum of all the signals generated from the activated cells.

The information given as output of the simulation are:

- **Data reported from GEANT4 simulation:** event ID, type of fibre, fibre ID, fibre position;

- **Computed quantities:** integral, peak height, time of arrival, time over threshold, time of peak;
- **Digitized waveform.**

All this features can be rejected through a trigger, in particular a threshold can be set to establish the informations that have to be recorded. The threshold is defined as a scale of the maximum value of a waveform generated by a single photoelectron (neglecting the electrical noise). In the results showed later a one-suppression has been applied using a threshold factor of 1.5, a typical setup to filter isolated signals of DCR.

## 5.2 Simulation performances

### 5.2.1 Different configurations

The results shown in this last chapter are obtained considering different SiPM parameters configurations.

They have been chosen in a common parameter space identified checking the lineup of SiPMs produced by Hamamatsy [4]. Two are the parameters that has been changed in our studies:

- the decay time constant of the signal, the chosen values are 10 *ns* and 50 *ns*;
- the pixel size, the chosen values are 10  $\mu m$ , 15  $\mu m$  and 25  $\mu m$ .

The other fixed values of parameters are listed in the table 5.2.

An example of waveform generated is plotted in figure 5.4 where is clear the difference produced using two different decay time constant.

### 5.2.2 Time studies

An important aspect that has to be studied is the temporal one. In order to do this, data of 1000 events are produced. In each event a 40 *GeV* electron is produced from the interaction point.

A first step is to analyze the distribution of the time of arrival of the photons converted at the SiPMs (i.e. the time recorded in the GEANT4 simulation output).

The distribution obtained from *C* and *S* photons are plotted in figure 5.5. As expected, the distribution of *C* photons time extremely narrow due to the instantaneous production of photons at the passage of relativistic charged particle in the fibres, instead the *S* photons time distribution shows an exponential tail that is a direct consequence of the emission time constant

Geometrical Parameter	
SiPM area	$1 \times 1 \text{ mm}^2$
Sensor Parameters	
DCR	$200 \text{ kHz}$
After-Pulse	3%
Cross-Talk	1%
Signal Parameter	
Rise time	$1 \text{ ns}$
Waveform Parameters	
Time window	$500 \text{ ns}$
Integration window	$300 \text{ ns}$
Sampling frequency	$10 \text{ GHz}$

Tabella 5.2: parameter

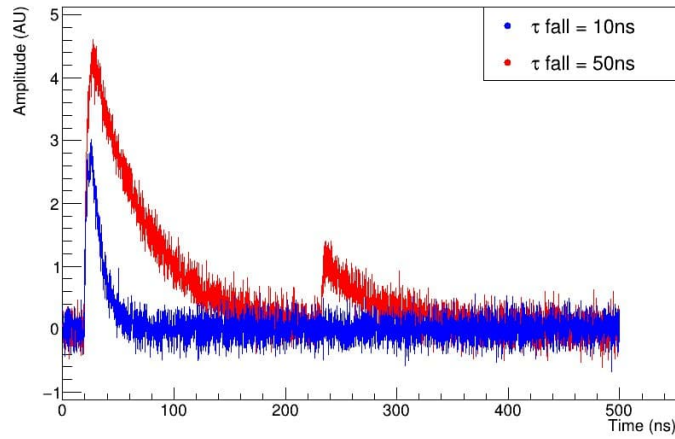


Figura 5.4: Single waveform

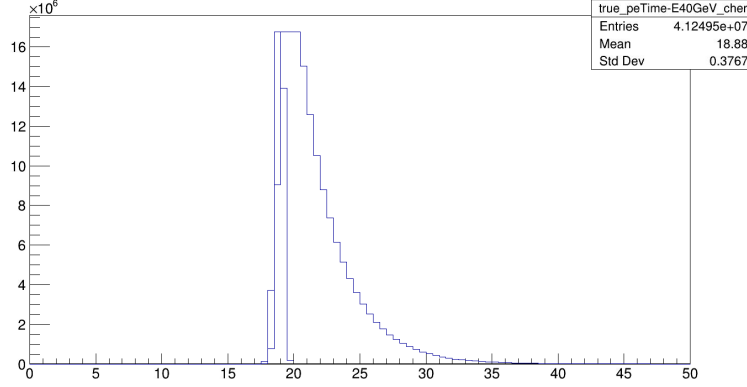


Figura 5.5: True time of arrival distribution.

of the Polystyrene.

Now a step forward can be done using this data as input for *pySiPM*. The SiPM parameters are chosen as described in paragraph 5.2.1. In this context the most interesting editable parameter is the decay time constant. Figure 5.6a and 5.6b are in analogy with respect to the last described and presents clearly a widening of the distributions, the cause of this phenomenon has to be associated to the characteristic response function of the sensors 5.3.

These data can be compared looking for differences in changing SiPMs configurations. As we can see in figure 5.7, the same *C* and *S* photons produce narrower time of peak distribution due to the less impact of electronic noise on a sharper response function.

The impact of noise on time of peak precision is also dependent on the number of photons impinging the same SiPM, in particular the peak precision increase with the number of photons.

To prove this 10000 SiPMs have been fired with an increasing number of simultaneous photons. For each fixed number of photons, the time of peak has been recorded, plotted in an histogram and fitted with a Gaussian function. An example of these histograms is shown in figure 5.8.

The standard deviation of these Gaussian fit is the interested quantity that has been recorded and reported in the table 5.3.

It is interesting to plot these data and study the behavior of the standard deviation in fuccion of the number of photons. Figure 5.9 shows graphically the data, which are well fitted with a function of the form:

$$\sigma = \frac{A}{\sqrt{n}} + B. \quad (5.4)$$



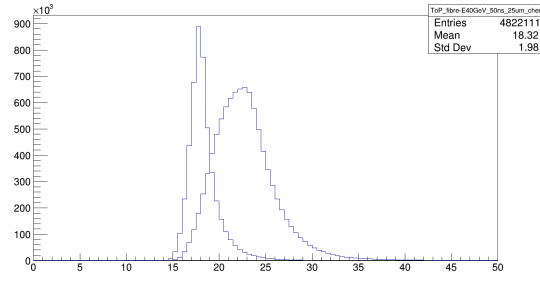
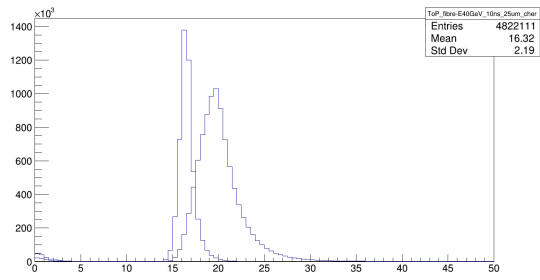
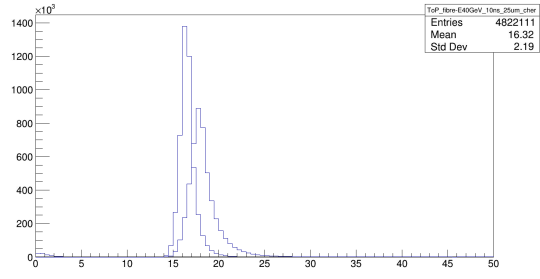
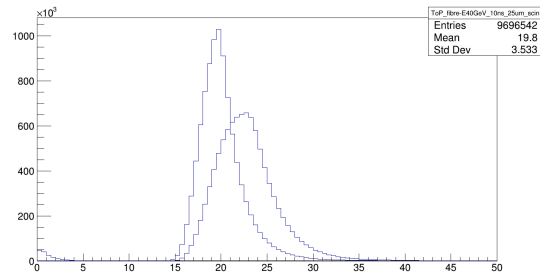
(a)  $\tau_{fall} = 50$  ns.(b)  $\tau_{fall} = 10$  ns.

Figure 5.6: time of peak distribution.



(a) C fibres.



(b) S fibres.

Figure 5.7: time of peak distribution.

Number of photons	$\sigma$ with $\tau_{fall} = 10 \text{ ns}$ [ns]	$\sigma$ with $\tau_{fall} = 50 \text{ ns}$ [ns]
1	1.4150	7.0680
2	0.8717	2.6420
3	0.6738	1.7370
4	0.5742	1.3770
5	0.5146	1.1230
6	0.4624	0.9719
7	0.4314	0.9148
8	0.3998	0.8508
9	0.3811	0.7717
10	0.3605	0.7169
25	0.2339	0.4481
50	0.1679	0.3112
100	0.1229	0.2297

Tabella 5.3: Sigmas

The parameters obtained are  $A = 0.8712 \text{ ns}$  and  $B = 0.08734 \text{ ns}$  for data associated to SiPMs with  $\tau_{fall} = 10 \text{ ns}$ , and  $A = 1.949 \text{ ns}$  and  $B = 0.008217 \text{ ns}$  for data associated to SiPMs with  $\tau_{fall} = 50 \text{ ns}$ .

### 5.2.3 Occupancy effect

The occupancy effect, as shown in the paragraph 4.1, is an important characteristic that has to be deeply studied to know the behaviour of the SiPMs under high number of impinging photons and to correctly reconstruct the released energy.

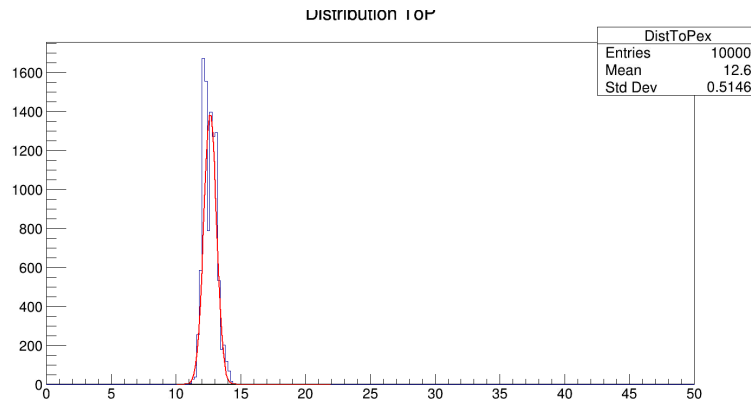


Figura 5.8: Time of peak dummy, 5 photons, 50 ns.

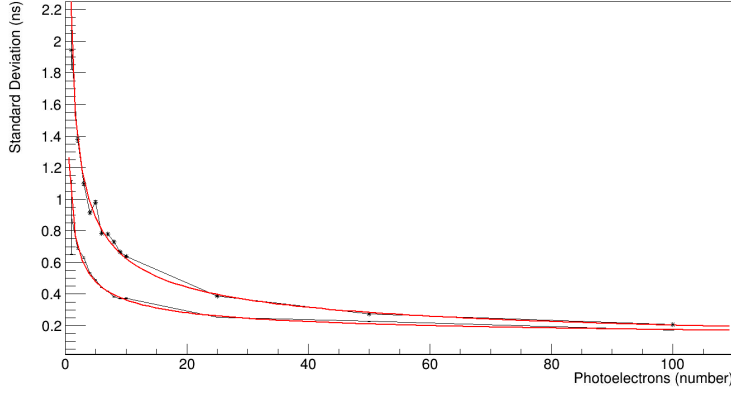


Figure 5.9: Time of peak dummy, 5 photons, 50 ns.

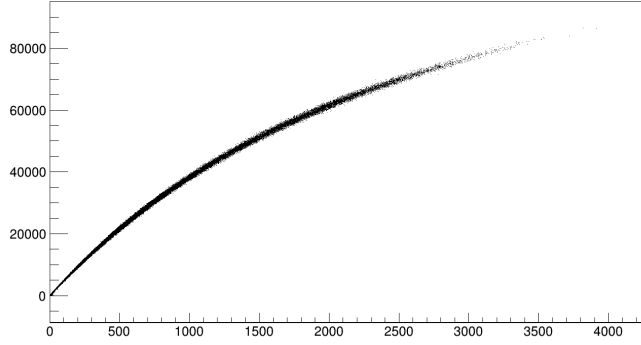


Figure 5.10: Saturation 40GeV 25um scin.

As can be seen in figure 5.10, this effect is reproduced correctly in our simulations. The example shows the charge integral in dependence to the number of p.e. and follows the concepts already seen in paragraph 4.2.1.

The first step to perform these studies is to reconstruct a calibration law that reproduces the charge integral with respect to the number of p.e. firing the same SiPM.

Starting by assuming that in the range of photoelectrons from 2 to 10 the saturation effect does not occur in our configurations (i.e. 10000, 4356 and 1600 cells in each SiPM), 10000 SiPM has been fired 9 times with an increasing number of simultaneous p.e. in the range considered.

To assume that no saturation effect occurs in these data the charge integral distribution from the three different configurations has been compared finding no bias as seen in figure 5.11. The mean and the RMS values has been recorded and fitted with a strait line corresponding to the calibration law desired:

$$I(n) = A \cdot n + B \quad (5.5)$$

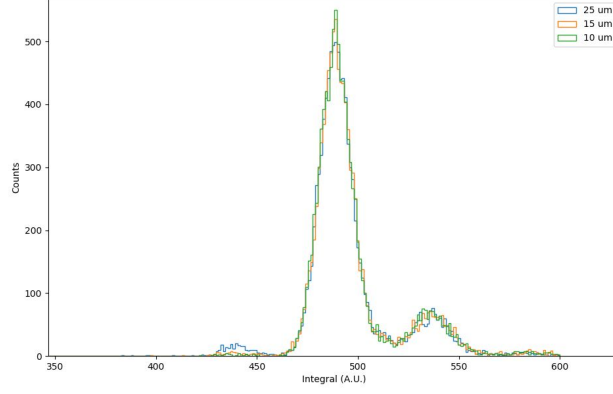


Figura 5.11: 10pe sat check.

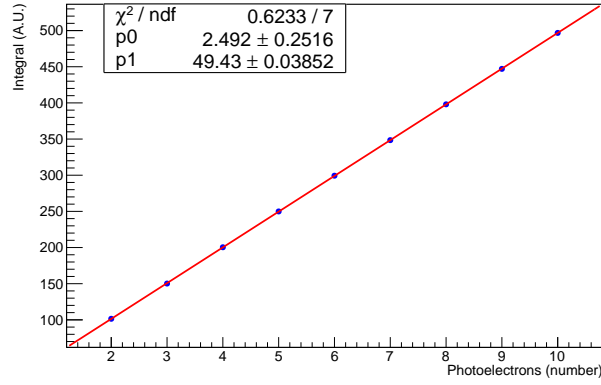


Figura 5.12: NoSatLine.

with  $A = 49.43 \pm 0.03852$  and  $B = 2.491 \pm 0.2516$  (fig 5.12).

The parameter  $A$  represents the contribution to the charge integral associated to a single photoelectron. Meanwhile  $B$  is the pedestal that is originated mostly by the DCR. This contribution can be evaluated considering our parameters of  $DCR = 200 \text{ kHz}$  and the integration window of  $300 \text{ ns}$ .  $B_{DCR} = 2 \cdot 10^5 \cdot 3 \cdot 10^{-7} \text{ p.e.} = 6 \cdot 10^{-2} \text{ p.e.} = 6 \cdot 10^{-2} \cdot 49.43 = 2.96$ . In the following result, the value of the pedestal has been subtracted to the integral value of each SiPM.

The occupancy effect has been studied in electromagnetic shower produced by single electrons of different energies at each event with discrete values of 20, 40, 60, 80  $\text{GeV}$ .

The impact of the saturation has been quantified using the line  $I = A \cdot n$  as no saturation reference. The result obtained from 10000 events of single

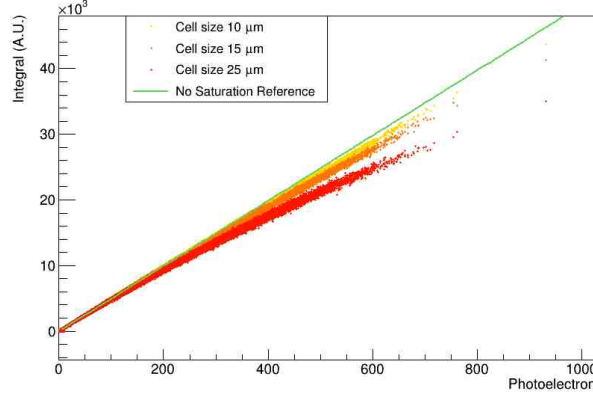
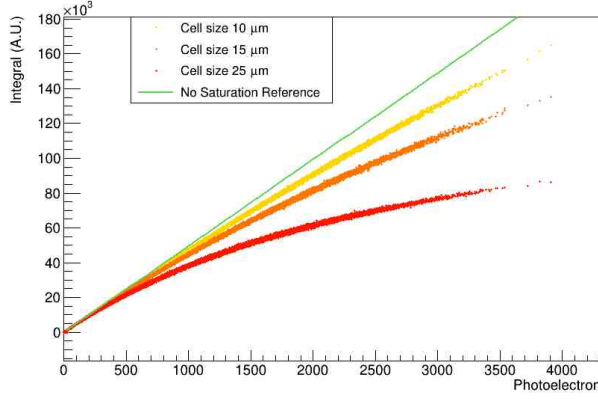
(a)  $C$  signals.(b)  $S$  signals.

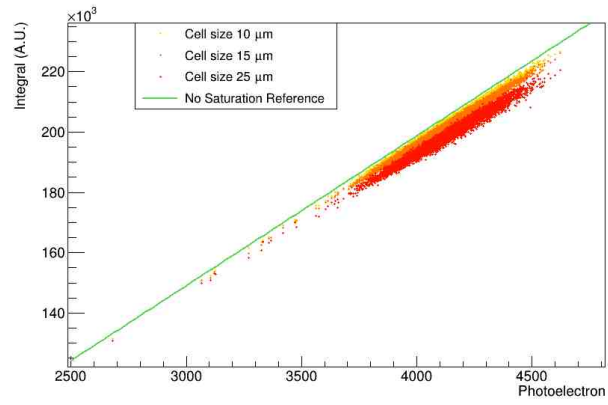
Figura 5.13: Saturation fibres.

$40 \text{ GeV } e^-$  with different SiPM configurations are separated in Cherenkov and Scintillation signals. They are shown in figure 5.13 where each point correspond to a single SiPM. The smaller is the number of cells, the greater is the occupancy effect.

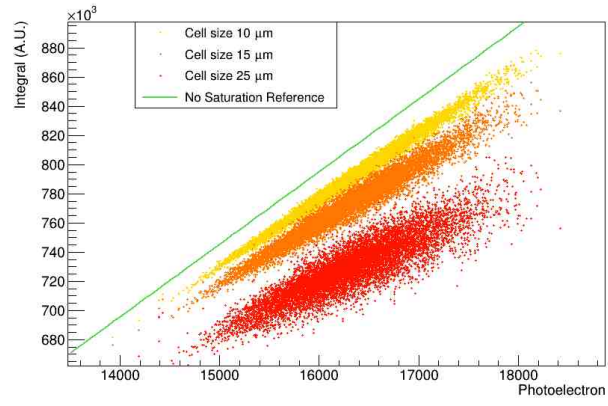
Moreover, as expected, the scintillation fibres transport  $\sim 4$  times the p.e. from Cherenkov ones on average, therefore they are more affected to the saturation.

This process can be extended considering one event at the time and adding the charge integral and the corresponding number of photoelectrons. The effect produced is represented in figure 5.16 where each point correspond to a single event.

As can be seen, the occupancy effect in our conditions is consistent. To



(a) *C* signals.



(b) *S* signals.

Figura 5.14: Saturation events.

mitigate this problem an analytical correction can be performed through the formula:

$$N_{fired} = N_{cells} \cdot \left[ 1 - \exp \left( -\frac{N_{p.e.}}{N_{cells}} \right) \right] \quad (5.6)$$

therefore the correction has been applied modifying the integral values such as:

$$I_{corr} = -AN_{cells} \left[ \ln \left( 1 - \frac{I}{AN_{cells}} \right) \right] \quad (5.7)$$

The results obtained can be visualized in figure 5.15 where are compared the data from SiPM with cell size of 10  $\mu m$  with and without analytical correction.

The discrepancy from the no saturation reference quantifies the effect of the occupancy when performing the energy reconstruction task. The percentage difference has been evaluated through the formula  $\frac{E_{NoSat} - E}{E_{NoSat}}$ , and the value obtained fill the histograms in figure 5.14.

After applying the analytical correction a clear improvement is show in figures 5.17.

This whole process has been performed simulating electrons with energies of 20, 40, 60, 80  $GeV$ . Mean and standard deviation of the gaussian fit applied on the percentage discrepancy have been recorded and the obtained plots are shown in figure 5.18.

#### 5.2.4 Energy resolution

The first step to study the energy resolution is to calibrate the full simulation.

Dual-readout calorimeters are typically calibrated at the electromagnetic scale. This is specially useful in a leptonic collider because, having easily access to electrons and positrons, the calorimeter can be calibrated precisely during all the life of the experiment.

The calibration has been performed on 40  $GeV$  electrons applying the one-suppression already introduce un paragraph 5.1.2. 10000 events with single 40  $GeV$  electrons have been fired from the interaction point obtaining the charge integral distributions for scintillation and Cherenkov signals shown in figure 5.19. The calibration constants obtained to transform these histograms in energy distributions centered around 40  $GeV$  are:  $k_S = 4.998 \times 10^{-5}$  and  $k_C = 2.023 \times 10^{-4}$ .

Two analogue calibration constants have been obtained starting from the number of photoelectrons distribution with values of:  $k_{pe,S} = 2.48 \times 10^{-3}$  and  $k_{pe,C} = 1.00 \times 10^{-2}$ .

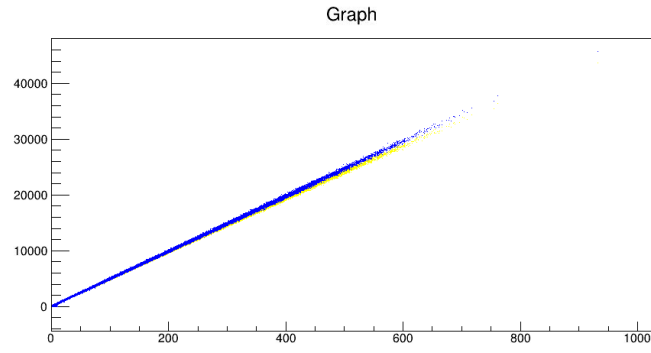
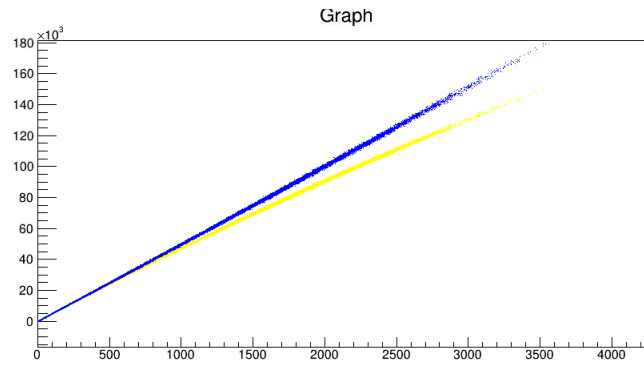
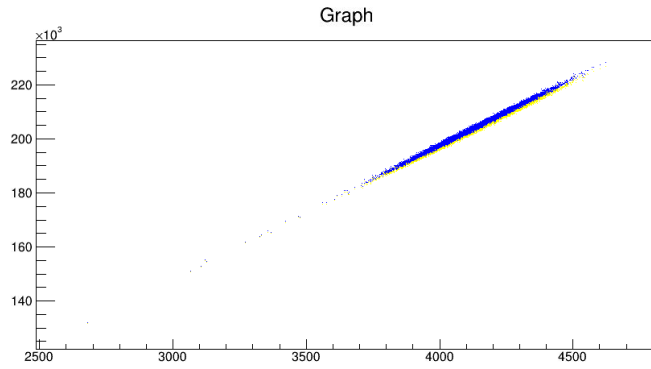
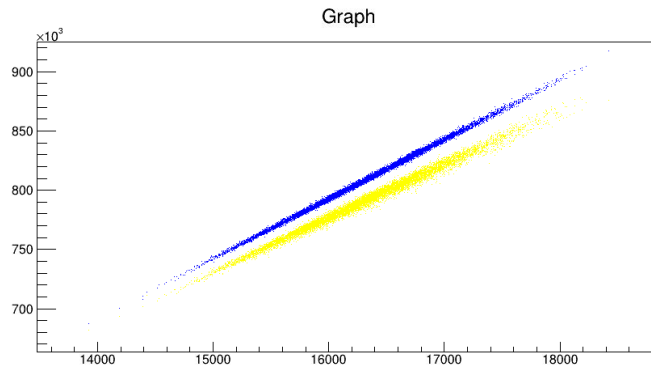
(a)  $C$  signals fibres.(b)  $S$  signals fibres.(c)  $C$  signals events.(d)  $S$  signals events.

Figura 5.15: Saturation with correction.



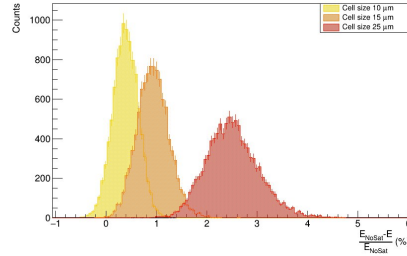
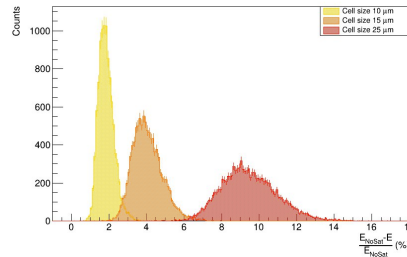
(a) *C* signals.(b) *S* signals.

Figure 5.16: Percentage discrepancy.

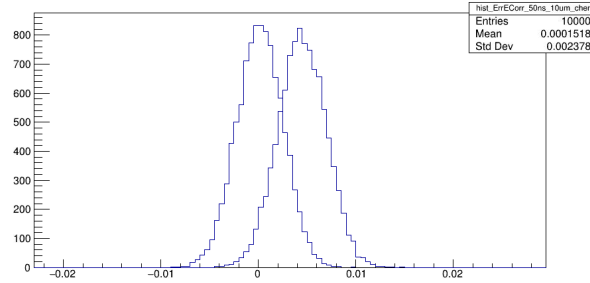
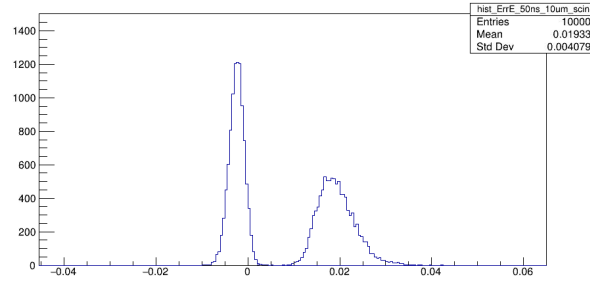
(a) *C* signals.(b) *S* signals.

Figure 5.17: Percentage discrepancy with correction.

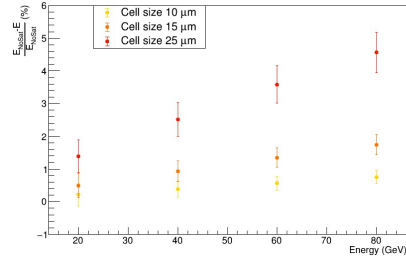
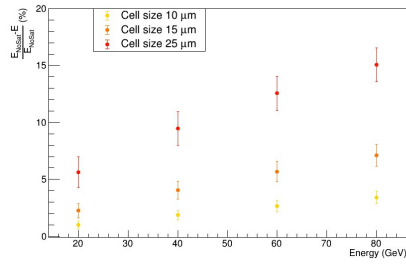
(a)  $C$  signals.(b)  $S$  signals.

Figura 5.18: Percentage discrepancy versus energy.

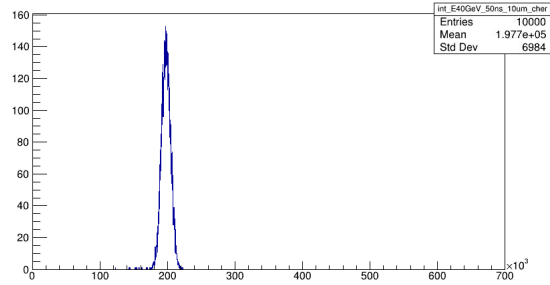
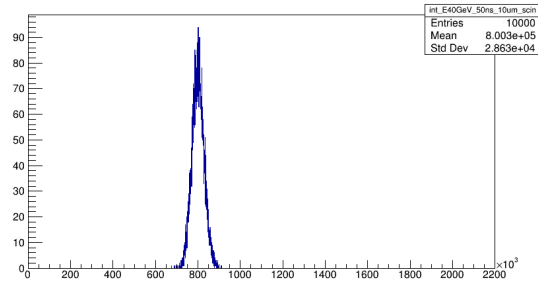
(a)  $C$  signals.(b)  $S$  signals.

Figura 5.19: Integral distrib.

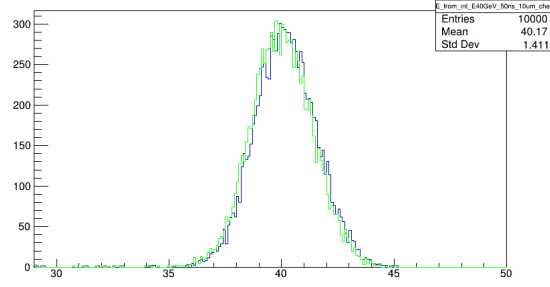
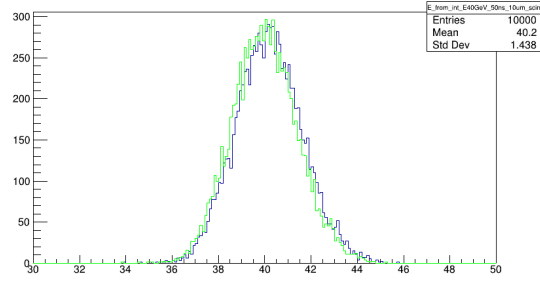
(a)  $C$  signals.(b)  $S$  signals.

Figure 5.20: Integral distrib.

Starting from these calibration constant, the energy distributions can be obtained from the number of p.e. (pre SiPM digitization simulation) or from the charge integral (post SiPM digitization simulation). The two types of distribution are compared in figure 5.20.

As expected, the energy distributions obtained from the charge integrals are wider due to the introduction of the electronic noise. However, the effect is minimal considering the fact that in each event hundreds of SiPMs are active and the white noise has mean zero.

The energy distributions have been fitted with a Gaussian function to obtain mean, standard deviation e respective errors. Doing this with different primary electron energies the energy resolution can be studied. Mean and standard deviation are listed in tables 5.4 5.5.

Then fitting the  $\sigma/E$  values in the energy range  $20 - 80 \text{ GeV}$  can be seen there is a good agreement with the functions:

$$\frac{\sigma}{E} = \frac{A_1}{\sqrt{E}} + B_1 \quad \text{or} \quad \frac{\sigma}{E} = \frac{A_2}{\sqrt{E}} \oplus B_2 \quad (5.8)$$

as shown in figure 5.21, with the fit parameters listed in table 5.6 and 5.7. The plots also show the loss of resolution with the introduction of the SiPM digitization software.

	True E (GeV)	Mean E (GeV)	Standard Deviation (GeV)
<b>Scintillation</b>	20	19.90	0.95
	40	40.00	1.44
	60	60.65	1.85
	80	81.18	2.26
<b>Cherenkov</b>	20	19.88	0.95
	40	40.00	1.42
	60	60.61	1.73
	80	81.12	2.08

Tabella 5.4: Sigmas

	True E (GeV)	Mean E (GeV)	Standard Deviation (GeV)
<b>Scintillation</b>	20	19.82	0.92
	40	40.00	1.39
	60	60.28	1.78
	80	81.58	2.16
<b>Cherenkov</b>	20	19.76	0.92
	40	40.00	1.36
	60	60.40	1.66
	80	81.86	1.91

Tabella 5.5: Sigmas

	<b>Scintillation</b>	<b>Cherenkov</b>
<b>pre pySiPM</b>	$\frac{17.39\%}{\sqrt{E}} + 0.37\%$	$\frac{21.13\%}{\sqrt{E}} + 0.01\%$
<b>post pySiPM</b>	$\frac{17.84\%}{\sqrt{E}} + 0.77\%$	$\frac{20.01\%}{\sqrt{E}} + 0.30\%$

Tabella 5.6: Regular sum

	<b>Scintillation</b>	<b>Cherenkov</b>
<b>pre pySiPM</b>	$\frac{19.78\%}{\sqrt{E}} \oplus 1.55\%$	$\frac{21.21\%}{\sqrt{E}} + 0.07\%$
<b>post pySiPM</b>	$\frac{20.14\%}{\sqrt{E}} \oplus 1.62\%$	$\frac{21.04\%}{\sqrt{E}} + 0.98\%$

Tabella 5.7: Quadratic sum

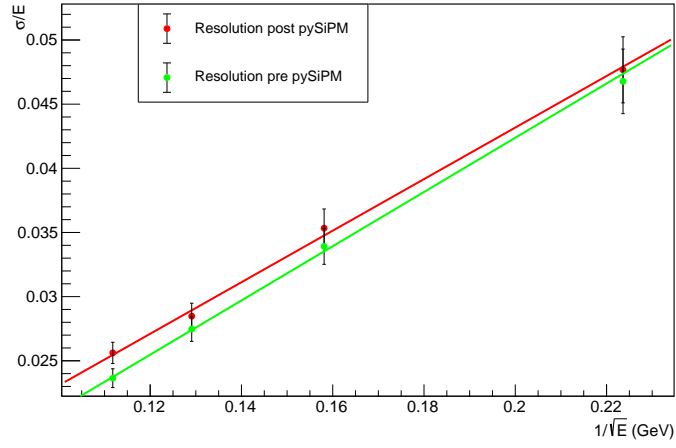
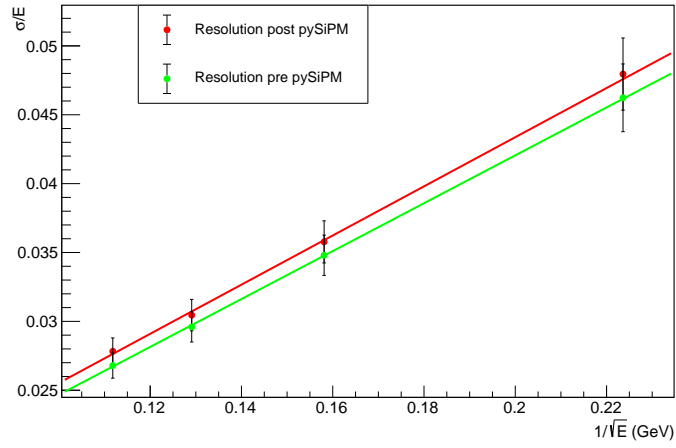
(a)  $C$  signals.(b)  $S$  signals.

Figure 5.21: Integral distrib.

## **5.3    Neural Network: Particle ID on waveform**

aaa

### **5.3.1    Configuration**

aaa

### **5.3.2    Performances**

aaa

## **5.4    Neural Network: Particle ID on imaging**

aaa

### **5.4.1    Configuration**

aaa

### **5.4.2    Performances**

aaa

## Capitolo 6

# Conclusion

aaa





# Thanks

aaa



# Bibliografia

- [1] Y. Fukuda et al., Phys. Rev. Lett. 81 (1998) 1158-1162.
- [2] Y. Fukuda et al., Phys. Rev. Lett. 81 (1998) 1158-1162.
- [3] Y. Fukuda et al., Phys. Rev. Lett. 81 (1998) 1158-1162.
- [4] Hamamatsu SiPMs lineup [https://www.hamamatsu.com/eu/en/product/optical-sensors/mppc/mppc\\_array/all\\_products/index.html](https://www.hamamatsu.com/eu/en/product/optical-sensors/mppc/mppc_array/all_products/index.html)